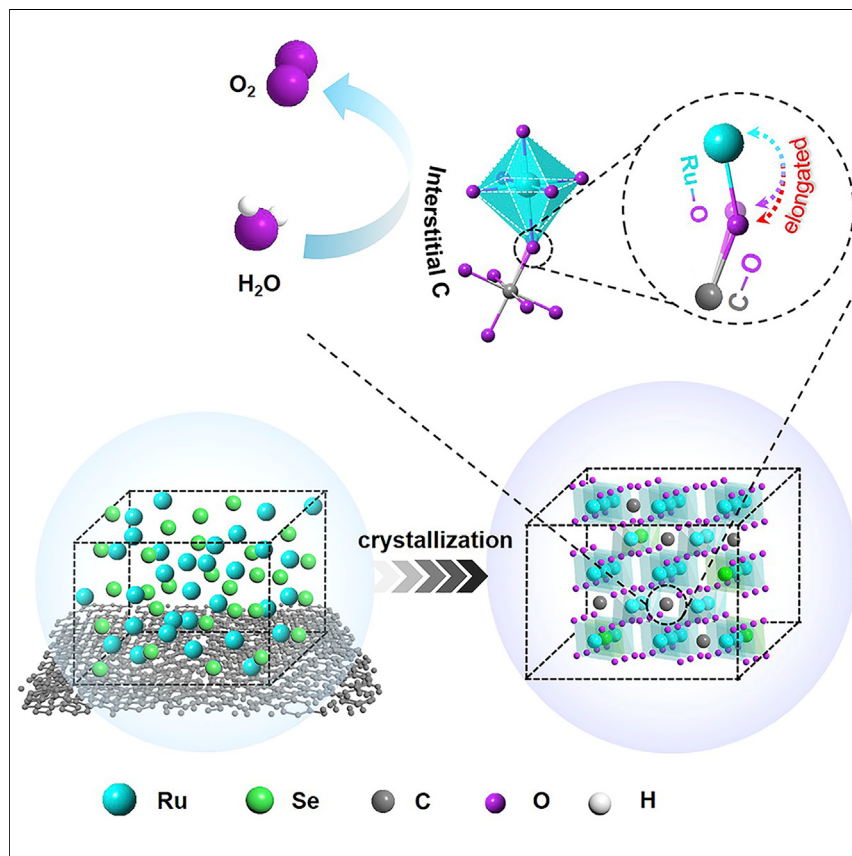


Article

Exceptionally active and stable RuO₂ with interstitial carbon for water oxidation in acid

A robust acidic OER electrocatalyst C-RuO₂-RuSe with interstitial carbon was designed and constructed by simultaneous Se evaporation and C combustion of the C-supported amorphous RuSe₂. Experimental and theoretical results prove that the interstitial C can elongate the Ru-O bonds to enhance the binding energy for *O and thus lead to a significant increase in stability. This project provides a new perspective to improve electrocatalytic OER stability under acidic conditions by inducing interstitial atoms.

Juan Wang, Chen Cheng, Qi Yuan, ..., Tao Cheng, Feng Jiao, Xiaoqing Huang

qshao@suda.edu.cn (Q.S.)
hxq006@xmu.edu.cn (X.H.)

Highlights

C-RuO₂-RuSe-10 exhibits long-term stability of up to 50 h under acidic environments

The existence of interstitial C will elongate the Ru-O bonds

The dissociation energy of *O will be enhanced by introducing the interstitial C

Article

Exceptionally active and stable RuO₂ with interstitial carbon for water oxidation in acid

Juan Wang,^{1,2,10} Chen Cheng,^{4,10} Qi Yuan,^{4,10} Hao Yang,⁴ Fanqi Meng,⁵ Qinghua Zhang,^{5,6} Lin Gu,^{5,6,7} Jianlei Cao,³ Leigang Li,¹ Shu-Chih Haw,⁸ Qi Shao,^{3,*} Liang Zhang,⁴ Tao Cheng,⁴ Feng Jiao,⁹ and Xiaoqing Huang^{1,11,*}

SUMMARY

Oxygen evolution reaction (OER) plays a critical role in energy conversion technologies. Significant progress has been made in alkaline conditions. In contrast, it remains a challenge to develop stable OER electrocatalysts in acidic conditions. Herein, we report a new strategy to stabilize RuO₂ by introducing interstitial carbon (C-RuO₂-RuSe), where the optimized C-RuO₂-RuSe-5 exhibits a low overpotential of 212, 259, and 294 mV to reach a current density of 10, 50, and 100 mA cm⁻², respectively. More importantly, C-RuO₂-RuSe-10 has long-term stability of up to 50 h, representing one of the most stable OER electrocatalysts. X-ray absorption spectroscopy reveals that the Ru–O bonds have been elongated due to the formation of interstitial C. Theoretical calculations show that the elongated Ru–O bonds in RuO₂ enhance its stability and reduce energy barriers for OER. This work provides a new perspective for designing and constructing efficient Ru-based electrocatalysts for water splitting.

INTRODUCTION

Electrochemical water electrolyzer, as a next-generation renewable energy conversion and storage device, is considered as a promising technology to alleviate environmental issues and energy crisis.^{1–5} In electrochemical water splitting, the anodic oxygen evolution reaction (OER) is thermodynamically uphill and sluggish in kinetics, usually resulting in large overpotentials to drive the practical process.^{6–9} As the benchmark electrocatalysts for OER, ruthenium oxide (RuO₂) and iridium oxide (IrO₂) have received overwhelming attention due to their excellent activity and relatively good stability under acidic environments.^{10–12} Although IrO₂ exhibits higher stability in acids than RuO₂ does, IrO₂ suffers from a relatively low OER activity and extremely low abundance.^{13–15} To this end, improving the corrosion resistance of Ru-based materials with relatively low cost under harsh environments is attractive, yet challenging.

The inherent electronic properties endow RuO₂ with moderate adsorption capacity for intermediates and thus outstanding OER activity; however, the formation of soluble RuO₄ species usually degrades the stability of RuO₂ when the anodic potential is higher than 1.4 V in the acidic OER process.¹⁶ Inhibiting the dissolution of RuO₂ by modulating the electronic structure and changing adsorption capacity may be an attractive strategy to overcome the above obstacles.^{17,18} In view of this, a heterostructured Ru@IrO_x with a strong charge redistribution between a strained Ru core

The bigger picture

Proton-exchange membrane (PEM) water electrolyzer, as a significant renewable energy conversion and storage device, has attracted a great deal of attention. However, the anodic oxygen evolution reaction is limited by the disadvantages of low stability under harsh operation conditions. Herein, a new strategy to stabilize RuO₂ as an acidic OER electrocatalyst by introducing interstitial carbon (C-RuO₂-RuSe) has been reported. Benefiting from the existence of interstitial C, the extension of the Ru–O bonds leads to an increase in the dissociation energy of *O, thereby significantly enhancing the OER stability of C-RuO₂-RuSe in an acidic environment.

Improving the stability of the state-of-the-art Ru-based materials is the long-term goal for a PEM water electrolyzer because of their cheap price and higher activity. This work opens a new horizon for designing and constructing efficient acidic OER electrocatalysts for a PEM device by introducing interstitial atoms.

and an IrO_x shell has been proposed as a potential OER electrocatalyst under acidic conditions.¹⁹ However, the improvement in stability is based on sacrificing activity. In addition, anchoring the dispersed Ru atoms on the metal supports has also been demonstrated as an effective strategy to modify the electronic structure and binding strength of intermediate species, thereby improving the acidic OER activity and stability.²⁰ Although the stability has been improved, it is still far from satisfactory for practical applications. The simultaneous realization of prominent enhancement on both activity and stability of OER electrocatalysts is still full of challenges, especially under harsh acidic conditions and oxidative environments.

Herein, we demonstrated that both stability and activity of RuO₂ can be improved simultaneously by introducing interstitial carbon (C-RuO₂-RuSe). The C-RuO₂-RuSe catalyst was prepared through the joint evaporation of Se and combustion of C. Specifically, the C-supported RuSe₂ hollow nanospheres (RuSe₂ HNSs) were heated for 5 and 10 h at 300°C in air atmosphere to generate C-RuO₂-RuSe-5 and C-RuO₂-RuSe-10, respectively. The optimized C-RuO₂-RuSe-5 exhibits an enhanced OER activity, substantially higher than that of commercial RuO₂. More importantly, C-RuO₂-RuSe-10 shows improved stability, which can endure up to 50 h at current densities of 10, 20, and 50 mA cm⁻² in 0.5 M H₂SO₄, representing one of the most stable acidic OER electrocatalysts reported in the literature. X-ray absorption spectroscopy (XAS) reveals that the interstitial C can elongate the Ru–O bonds and thus it significantly improves the stability. Theoretical calculations further show that the interstitial C-activated Ru site can improve the OER performance. Therefore, both experimental and theoretical results prove that RuO₂ can be stabilized by introducing interstitial C and thus can be used as a robust acidic OER electrocatalyst.

RESULTS AND DISCUSSION

Catalyst synthesis and characterization

The initial RuSe₂ HNSs were synthesized through a hydrothermal method, where hexaaammineruthenium (III) chloride (Cl₃H₁₈N₆Ru) and selenious acid (H₂SeO₃) were reduced using hydrazine hydrate aqueous solution (N₂H₄·H₂O). The resulting RuSe₂ HNSs exhibit a hollow nanosphere shape with uniform size distribution in which the high contrast area in the high-angle annular dark-field scanning transmission electron microscopy (HAADF-STEM) image is the outer wall of the hollow sphere and the low contrast area is the hollow portion (Figure S1A). The enlarged TEM image shows that the hollow sphere comprises small nanoparticles as building blocks (Figure S1B). The atomic ratio of Ru/Se was determined to be about 1:2 by TEM energy-dispersive X-ray spectrophotometer (TEM-EDS), consistent with the results of inductively coupled plasma atomic emission spectrometry (ICP-AES) (Figure S1C). The crystalline structure of RuSe₂ HNSs was examined by powder X-ray diffraction (PXRD), and only an inconspicuous broad peak at ~30° was observed, revealing the amorphous nature of RuSe₂ HNSs (Figure S1D). Additionally, no obvious lattice fringes could be observed by high-resolution TEM (HRTEM), confirming that the RuSe₂ HNSs are amorphous, in agreement with the selected area electron diffraction (SAED) pattern and PXRD result (Figure S1E and S1F). A structure model of RuSe₂ HNSs with Ru and Se atoms disorderly arranged without long-range periodicity is shown in Figure S1G. Furthermore, scanning transmission electron microscopy energy-dispersive X-ray spectrophotometer (STEM-EDS) elemental mappings analysis confirms that Ru and Se are distributed uniformly across the whole HNS (Figure S1H).

RuSe₂ HNSs were loaded on Vulcan XC-72R C powder (Figure S2) and then thermally treated at 300°C in air for 10 h to generate C-RuO₂-RuSe-10. The HAADF-STEM and

¹State Key Laboratory of Physical Chemistry of Solid Surfaces, College of Chemistry and Chemical Engineering, Xiamen University, Xiamen, Fujian 361005, China

²Key Laboratory of Carbon Materials of Zhejiang Province, College of Chemistry and Materials Engineering, Wenzhou University, Wenzhou, Zhejiang 325035, China

³College of Chemistry, Chemical Engineering and Materials Science, Soochow University, Suzhou, Jiangsu 215123, China

⁴Institute of Functional Nano & Soft Materials (FUNSOM), Jiangsu Key Laboratory for Carbon-Based Functional Materials and Devices, Soochow University, Suzhou, Jiangsu 215123, China

⁵Beijing National Laboratory for Condensed Matter Physics, Institute of Physics, Chinese Academy of Sciences, Beijing, Xicheng 100190, China

⁶School of Physical Sciences, University of Chinese Academy of Sciences, Beijing, Xicheng 100049, China

⁷Songshan Lake Materials Laboratory, Dongguan, Guangdong 523808, China

⁸National Synchrotron Radiation Research Center (NSRRC), 101 Hsin-Ann Road, Hsinchu Science Park, Hsinchu 30076, Taiwan

⁹Center for Catalytic Science and Technology, Department of Chemical and Biomolecular Engineering, University of Delaware, Newark, DE 19716, USA

¹⁰These authors contributed equally

¹¹Lead contact

*Correspondence: qshao@suda.edu.cn (Q.S.), hxq006@xmu.edu.cn (X.H.)

<https://doi.org/10.1016/j.chempr.2022.02.003>

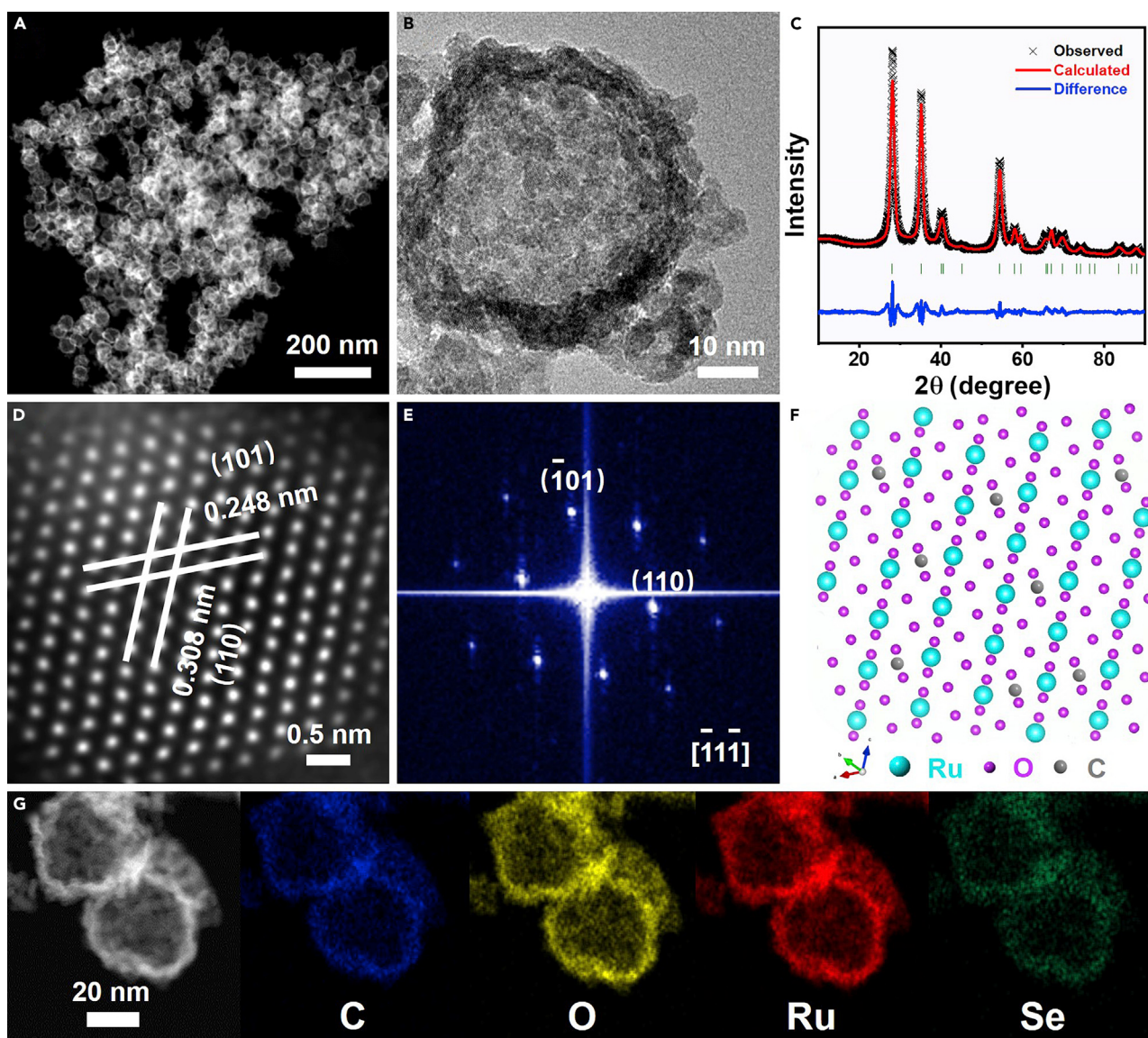


Figure 1. Morphology and structural characterizations

(A) HAADF-STEM image, (B) TEM image, (C) PXRD pattern, (D) high-resolution HAADF-STEM image, (E) FFT pattern, (F) crystal structure model, and (G) STEM image and STEM-EDS elemental mappings of C-RuO₂-RuSe-10. See also Figures S1–S5.

TEM images reveal that C-RuO₂-RuSe-10 maintains the hollow sphere morphology (Figures 1A and S3). The magnified TEM image shows that obvious lattice fringes can be observed in HNSs surrounded by nano-sized grains, indicating improved crystallinity by the heat treatment (Figure 1B). The PXRD pattern of C-RuO₂-RuSe-10 shows a set of distinct diffraction peaks corresponding to the tetragonal RuO₂, indicating that the crystal phase has changed from amorphous RuSe₂ to crystalline RuO₂ (Figure 1C). The unit cell parameter was obtained from PXRD by using the Rietveld refinement, indicating that the Se replaced part of Ru atoms and C located in the gaps of RuO₂ (Table S1). Lattice fringes can be observed clearly in HNSs in a spherical aberration-corrected HAADF-STEM image, where the interplanar spacings are 0.248 and 0.308 nm, and lattice shrinkage has occurred compared with the (101) and (110) planes of RuO₂ (Figure 1D). The corresponding fast Fourier transform

(FFT) pattern confirmed the crystalline nature of C-RuO₂-RuSe-10, where the exposed (110) and (101) planes along [111] zone axis are observed ([Figure 1E](#)). The crystal structure model along the [111] direction of RuO₂ shows that the Ru and O atoms are arranged in a tetragonal structure (P42/mnm) and C atoms are located in the space to form interstitial C, thus resulting in lattice deformations, matching well with the aberration-corrected HAADF-STEM image ([Figure 1F](#)). The TEM-EDS spectrum of C-RuO₂-RuSe-10 suggests that the atomic ratio of Ru/Se is 90.4:9.6 ([Figure S4](#)). The decrease of Ru/Se atomic ratio from RuSe₂ HNSs (37.6:62.4) to C-RuO₂-RuSe-10 (90.4:9.6) indicates the removal of Se element, which is likely caused by the volatilization of Se during heat treatment. As shown in the [Figures 1G](#), [1C](#), and [1O](#), Ru and Se elements are all uniformly distributed across the HNSs, confirming that Se and C are indeed introduced into RuO₂. No obvious C shell was observed in the HRTEM image of C-RuO₂-RuSe-10, indicating that the C has entered the interior of RuO₂ ([Figure S5](#)).

To systematically investigate the effect of heat treatment time on RuSe₂ HNSs, detailed characterizations of TEM, TEM-EDS, and PXRD were carried out to demonstrate the morphology, chemical composition, and crystal structure of RuSe₂ HNSs, respectively, treated for different time periods. As shown in [Figures S6–S10](#), when the heat treatment time increased from 0.5 to 30 h, the hollow spherical shape is largely maintained throughout the heat treatment process, whereas the atomic ratio of Ru/Se is significantly reduced from the original 37.6:62.4 (RuSe₂ HNSs) to 79.5:20.5 (C-RuO₂-RuSe-0.5), indicating that the Se element volatilizes rapidly during the heat treatment in air. The evaporation degree of Se element gradually slows down as the calcination time is further extended. PXRD patterns and Raman spectra analysis display that RuSe₂ is transformed into RuO₂ and its crystallinity can be improved as the treatment time increases ([Figures S11](#) and [S12](#)).^{21,22} The absence of the typical Raman signal (D band and G band) of the graphite C proves that the graphite structure is destroyed after heat treatment for 10 h. Thermal gravimetric (TG) curve of RuSe₂ HNSs reveals that a significant weight loss of about 27.7% occurred in the first 2 h, which is mainly caused by the rapid evaporation of Se under heating conditions; this is in good agreement with the TEM-EDS results ([Figures S6](#), [S7](#), and [S13](#)). Another slow weight loss appeared when the sample was thermally treated at 300°C from 2 to 10 h, which may be due to the slow diffusion of Se in crystalline RuO₂. However, this process was accelerated by the presence of Vulcan XC-72R C, and conversely, the volatilization process of Se also accelerated the combustion of C powder, which was verified by the almost disappearance of C powder in TEM images, as well as the absence of D band and G band in Raman spectra ([Figures S3](#), [S8–S10](#), and [S12](#)). From the TG curve of RuSe₂ HNSs (blue line), we found that the weight loss is negligible, which means that only a small amount of Se is lost after heat treatment for 10 h. In addition, the atomic ratio of C/O/Ru/Se was determined to be about 12:53:26:9 by ICP-AES and TG analysis. Similarly, the TEM image of Se-free catalysts exhibits a large amount of C powder, which also confirms that the presence of Se can indeed accelerate the combustion of C ([Figure S14](#)). In the absence of Vulcan XC-72R C, the hollow nanospheres collapsed, indicating that the presence of C improved the structural integrity of RuO₂ during Se evaporation and C combustion processes ([Figure S15](#)). Ultimately, the weight loss gradually decreased after heat treatment for 10 h, indicating that the interstitial C does exist and will escape as the heat treatment time increases.

Electronic structure investigation

To explore the influence of the presence of Se and C, XAS is employed to investigate the atomic structure and coordination environment. In detail, Ru K-edge X-ray

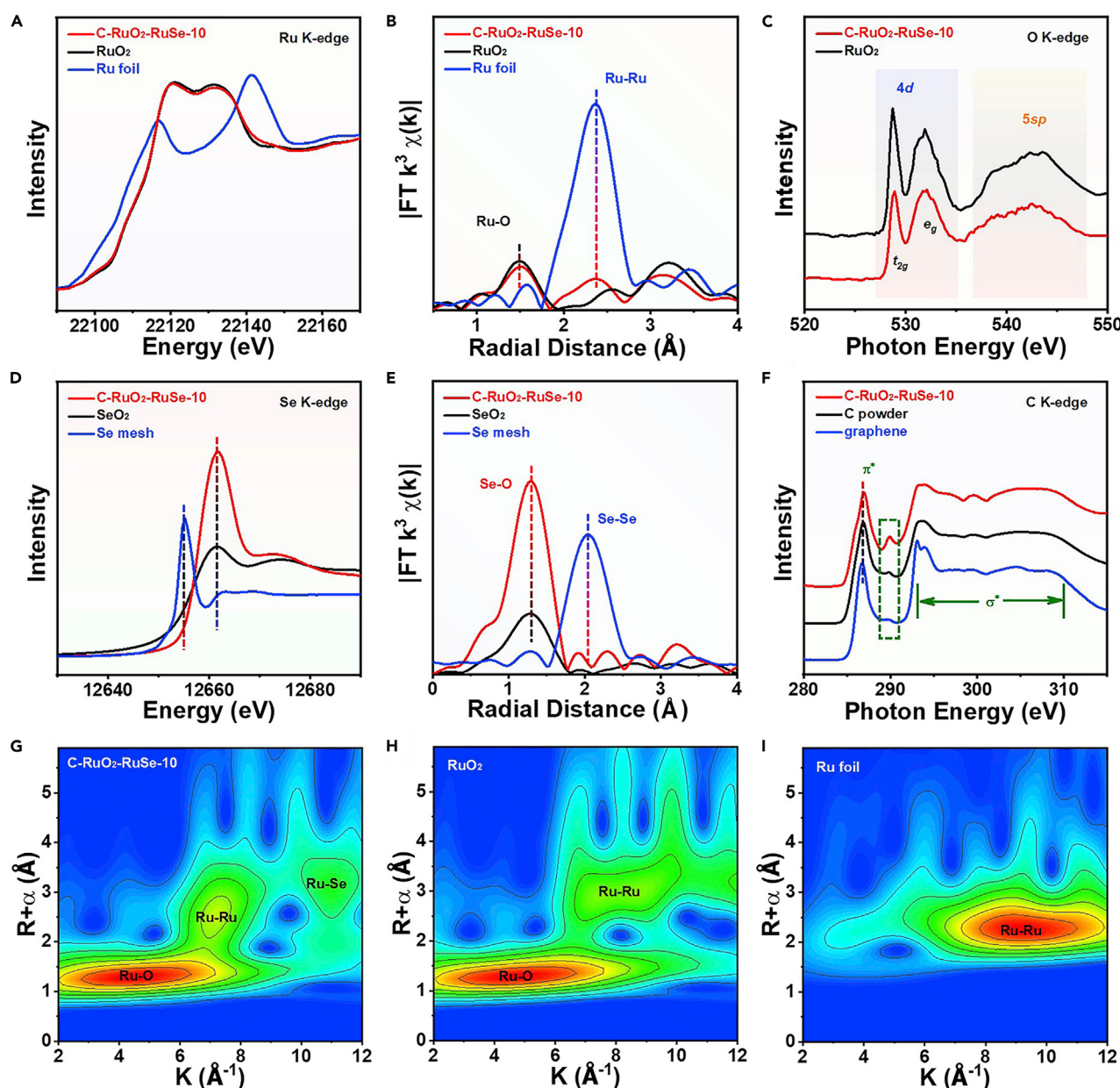


Figure 2. Electronic structure investigation

(A) Ru K-edge XANES, (B) Ru K-edge EXAFS, (C) O K-edge XANES, (D) Se K-edge XANES, (E) Se K-edge EXAFS, and (F) C K-edge XANES spectra of C-RuO₂-RuSe-10 and corresponding references.

Wavelet transform of Ru K-edge EXAFS data of (G) C-RuO₂-RuSe-10, (H) commercial RuO₂, and (I) Ru foil. See also Figures S6–S18 and Tables S1–S3.

absorption near edge structure (XANES) spectra show that the adsorption threshold position of C-RuO₂-RuSe-10 is considerably higher than that of Ru foil but close to that of commercial RuO₂, revealing that Ru in C-RuO₂-RuSe-10 presents an oxidation state of +4 (Figure 2A).^{23,24} Compared with RuO₂, the Fourier transforms of Ru K-edge extended X-ray absorption fine structure (EXAFS) spectra show that the Ru–O bonds of C-RuO₂-RuSe-10 shift to longer interatomic distance due to the slightly elongated Ru–O bonds by the formation of C–O bonds of interstitial C (Figure 2B). In addition, the intensity of Ru–O bonds of C-RuO₂-RuSe-10 is slightly weaker than that of RuO₂, indicating that the coordination environment is

unsaturated, which is caused by the presence of a small amount of oxygen vacancies (O_V); this is consistent with the curve fitting analysis of the Ru K-edge EXAFS spectra. The weak Ru–Ru bond is caused by the bonding between coordination-unsaturated Ru and adjacent Ru due to the existence of defect. The existence of defects, such as O_V and coordination-unsaturated Ru, has been confirmed to be effective for OER performance.^{25,26} In addition, the coordination configuration of Ru can be proved by fitting the EXAFS spectra (Figure S16; Table S2). For RuO₂, two sharp characteristic peaks at 528.7 and 531.9 eV are assigned to the excitation of O 1s core electrons into hybridized states between O 2p and Ru 4d t_{2g} and e_g states because of the splitting of an octahedral field (Figure 2C).²⁶ Another broad peak at higher energy is caused by the hybridization of the O 2p orbital with Ru 5sp states.²⁷ A similar O K-edge XANES spectrum was observed for C-RuO₂-RuSe-10, but the t_{2g}/e_g intensity ratio decreases from 0.42 (RuO₂) to 0.36, revealing the lower degree of hybridization and weaker covalency between O 2p and t_{2g} orbitals.²⁸ The Se K-edge XANES spectrum of C-RuO₂-RuSe-10 shifts to higher energy position than Se foil but line in the same position as SeO₂, indicating that the Se presents an oxidation state of +4 in C-RuO₂-RuSe-10 (Figure 2D). Subsequently, the corresponding Fourier transforms of EXAFS spectra show that the length of Se–O bonds in C-RuO₂-RuSe-10 is similar to that of SeO₂, and no Se–Se distance is observed (Figure 2E). Importantly, the EXAFS fitting results show that the coordination number of Se–O in C-RuO₂-RuSe-10 is nearly identical to that of Ru–O but significantly higher than that of SeO₂, indicating that Se atoms replaced part of Ru atoms to form an octahedral configuration with six coordination atoms (Figure S17; Table S3). As shown in Figure 2F, a sharp peak can be observed at about 286.8 eV in C K-edge XANES spectra, corresponding to the π^* antibonding state of C=C.²⁹ Additionally, a series of striking characteristic peaks between 293 and 310 eV can be assigned to the σ^* region.³⁰ Compared with graphene and C powder, a significantly enhanced peak appears (grass green color-dotted frame), which is caused by the C–O bond that is formed by interstitial C. The enhanced intensity and positive shift of binding energy of C–O suggest that the interstitial C in RuO₂ octahedrons will lead to a much stronger C–O binding. The shift of binding energy of Ru 3d demonstrates that the formation of interstitial C will generate the strong electronic interactions in C-RuO₂-RuSe-10 (Figure S18). The wavelet transform analysis exhibits that the Ru–O coordination intensity in C-RuO₂-RuSe-10 reaches the maximum at about 2.8~6.3 Å⁻¹, consistent with the results of RuO₂ but significantly different from those of Ru foil (Figures 2G–I). Importantly, a maximum intensity appears at about 10.0~11.9 Å⁻¹ that arises from the Ru–Se bond in C-RuO₂-RuSe-10.

Mechanism exploration

In view of the experimental analysis, a possible evolution process of C-RuO₂-RuSe-10 has been depicted. As illustrated in Figure 3, the C combustion can be accelerated and accompanied by the release of energy when the RuSe₂ HNSs are supported on Vulcan XC-72R C and then calcined at 300°C in air. Simultaneously, the long-range disordered Se atoms sublime with vacancies left, and thus, more free-volume zones are formed. Subsequently, oxygen atoms diffuse across the loosely bonded atomistic free-volume zones and combine with Ru atoms to form Ru–O bonds. Rearrangement and crystallization occur with the extension of calcination time, and thus, tetragonal RuO₂ with an octahedral structure is formed by further ripening, where Ru is located at the center and O site at the vertex. At that time, the remaining Se atoms will occupy part of Ru atoms to form an octahedral configuration with six coordination atoms, while the C atoms are trapped in the gap as interstitial C. Moreover, Vulcan XC-72R C with graphite structure is destroyed, and only a small amount of C remains as the calcination time increases. The Ru–O bonds are

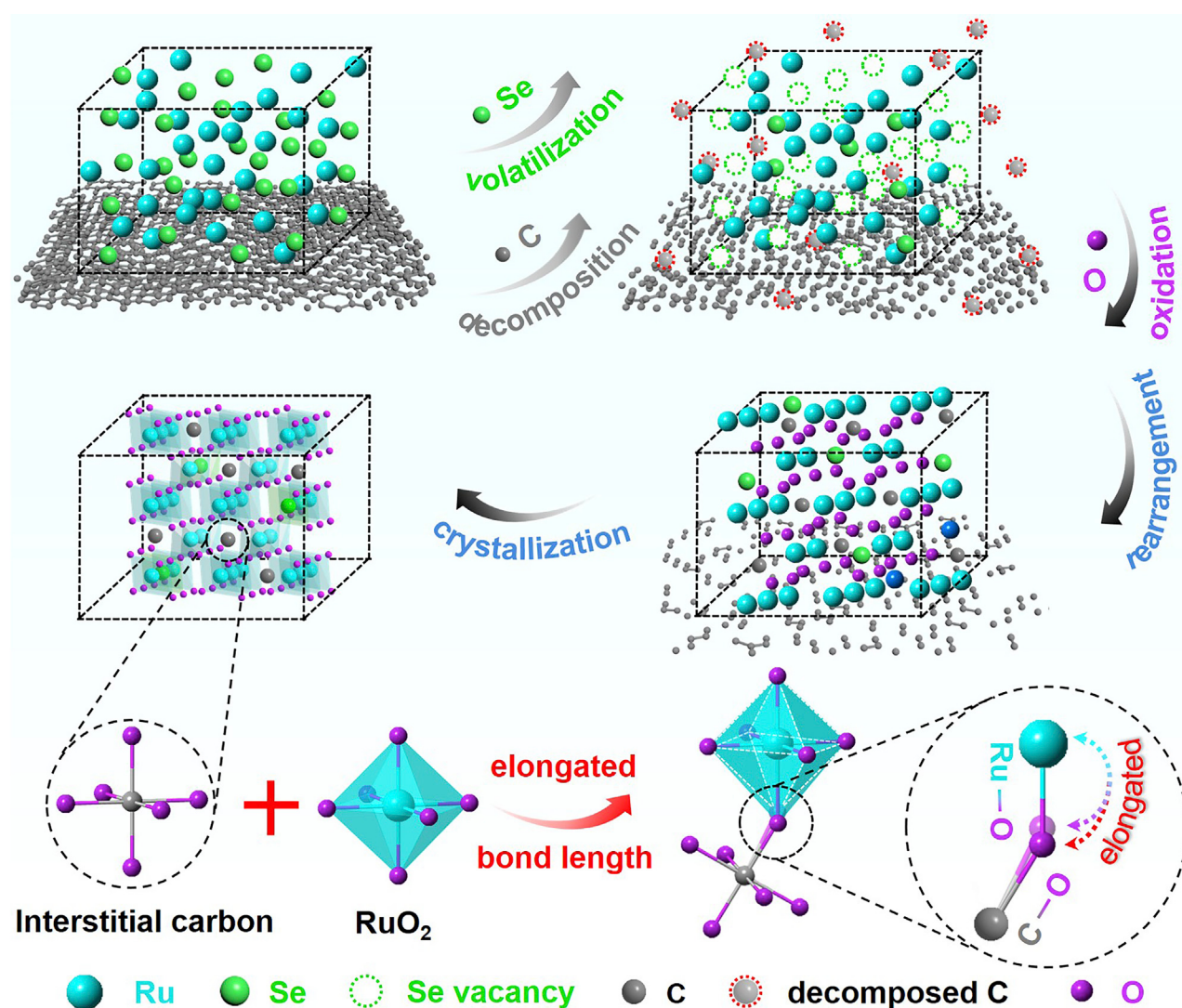


Figure 3. Schematic illustration

The formation process of C-RuO₂-RuSe-10.

elongated due to the C–O bonds formed by interstitial C, and therefore, the compression of the lattice fringes is observed by the atomic-resolution HAADF-STEM image. Additionally, the elongated Ru–O bonds were also directly measured by the Fourier transforms of the Ru K-edge EXAFS spectrum. The existing interstitial C atoms in the gaps of RuO₂ octahedrons will combine with the O atoms to generate C–O bonds; thus, the Ru–O bonds are elongated to improve catalytic activity and stability.

Evaluation of electrocatalytic performance

The unique structure of C-RuO₂-RuSe stimulates us to explore its potential applications for OER in acidic conditions. The OER performance was measured in 0.5 M H₂SO₄ with a typical three-electrode system at room temperature. All potentials were measured against the reversible hydrogen electrode (RHE) through the calibration of the saturated calomel electrode (SCE), which is a reference electrode (Figure S19). The benchmark commercial RuO₂ was also measured under the same

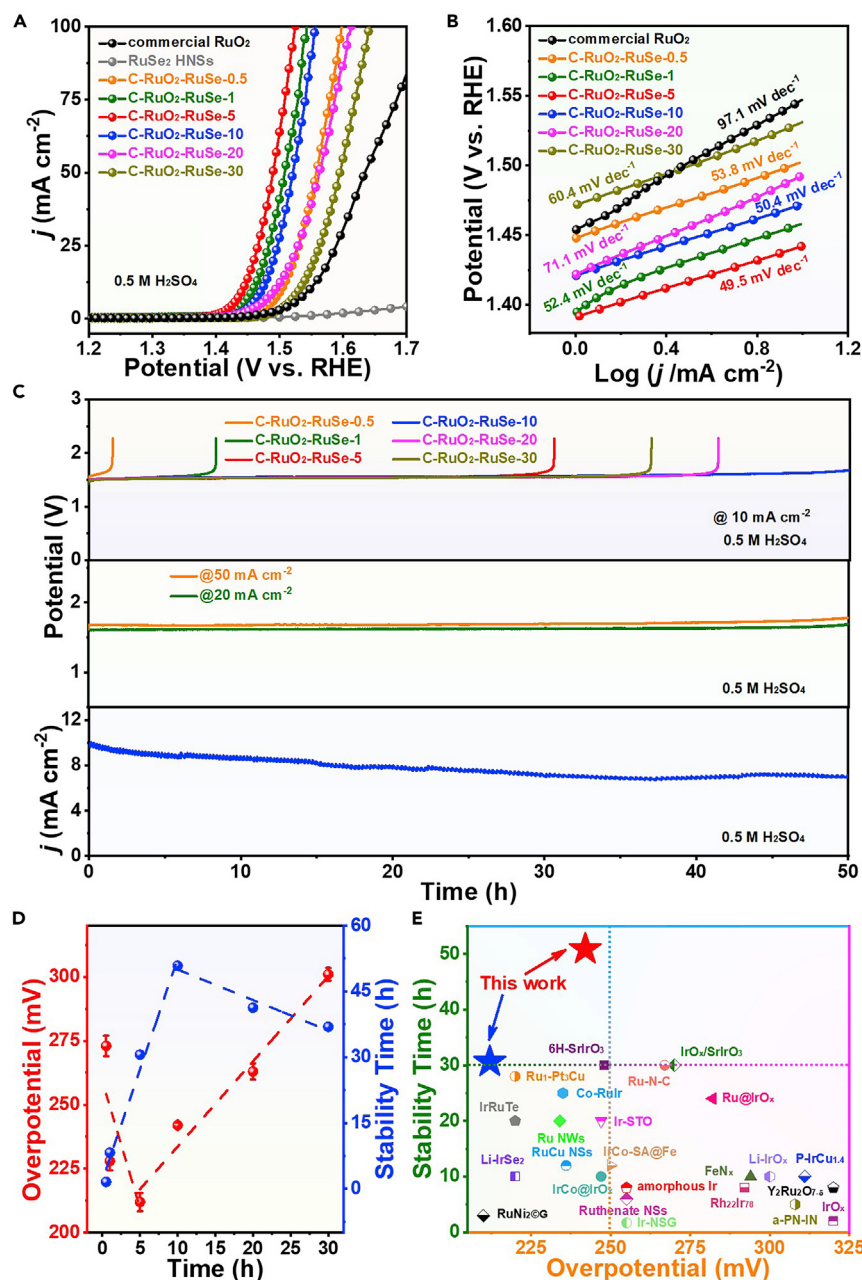


Figure 4. Electrochemical performance

(A and B) (A) OER polarization curves of various catalysts and (B) corresponding Tafel plots.
 (C) Chronopotentiometry tests of various C-RuO₂-RuSe catalysts at a constant current density of 10 mA cm^{-2} and C-RuO₂-RuSe-10 at constant current densities of 20 and 50 mA cm^{-2} , as well as chronoamperometry test of C-RuO₂-RuSe-10.
 (D) Heat treatment time-dependent overpotential and stability of various catalysts.
 (E) Comparison of the overpotential and stability of C-RuO₂-RuSe-5 and C-RuO₂-RuSe-10 with recently reported OER electrocatalysts in acidic media. See also Figures S19–S39 and Table S4.

conditions for comparison. The RuSe₂ HNSs exhibited low OER activity, while C-RuO₂-RuSe exhibited significantly high OER activity in acidic media, suggesting that the heat treatment of C-supported RuSe₂ HNSs under air environments plays a pivotal role in enhancing the OER performance (Figure 4A). Compared with

commercial RuO₂ (317, 404, and 498 mV at current densities of 10, 50, and 100 mA cm⁻², respectively), C-RuO₂-RuSe-5 requires a low overpotential of 212, 259, and 294 mV to reach the same current density. A similar trend was observed in 0.05 M H₂SO₄, where C-RuO₂-RuSe-5 requires an overpotential of 221 mV to achieve 10 mA cm⁻², superior to that of commercial RuO₂ ([Figure S20](#)). To evaluate the catalytic kinetics of OER, Tafel plots are obtained based on the polarization curves ([Figures 4B](#) and [S21](#)), where C-RuO₂-RuSe exhibits lower Tafel slopes than RuSe₂ HNSs do, indicating the enhanced OER kinetics after heat treatment.

Subsequently, the chronopotentiometry test of C-RuO₂-RuSe was performed in 0.5 M H₂SO₄ at 10 mA cm⁻² to assess the stability. For comparison, RuSe₂ HNSs and commercial RuO₂ were measured under identical conditions ([Figures S22](#) and [S23](#)). The stability of various C-RuO₂-RuSe has been significantly enhanced compared with RuSe₂ HNSs, demonstrating that the post-annealing treatment process in air can effectively improve the stability ([Figure 4C](#)). The best stability was achieved after heat treatment for 10 h. For example, C-RuO₂-RuSe-10 maintained the activity without any obvious decay for about 50 h under highly acidic conditions, substantially better than that of commercial RuO₂. Importantly, C-RuO₂-RuSe-10 can still operate stably for 50 h under harsh acidic media even at current densities of 20 and 50 mA cm⁻², representing excellent acidic OER stability. Additionally, the stability was also verified by chronoamperometry, where the current density of C-RuO₂-RuSe-10 decayed slowly, demonstrating excellent stability ([Figures 4C](#) and [S24](#)). Compared with commercial RuO₂, only slight degradation can be observed after the OER test, demonstrating the improved stability of C-RuO₂-RuSe-10 ([Figure S25](#)). The semicircle radius of C-RuO₂-RuSe-10 that is smaller than that of RuSe₂ HNSs and commercial RuO₂ in electrochemical impedance spectroscopy (EIS) indicates the lowest electric resistance and fastest electron transfer after introducing interstitial C ([Figure S26](#)). The nearly 100% Faraday efficiency (FE) proves that the high currents are derived from the OER process rather than the self-oxidation of the catalysts ([Figure S27](#)).³¹ To evaluate the effects of residual Se on the stability for OER, electrochemical leaching was performed, as shown in [Figure S28](#). The atomic ratio of Se decreased to 0.3%, and no obvious change of potential within 50 h was observed, indicating that the residual Se displays negligible effects on the durability test for OER. The correlation between structural and catalytic properties of C-RuO₂-RuSe and heat treatment conditions is summarized in [Figures 4D](#) and [S29](#), in which an inverted volcano-like OER activity—as a function of the heat treatment time—is evident and the C-RuO₂-RuSe-5 is located on top of the volcano exhibiting the best OER activity. The stability of the C-RuO₂-RuSe can be significantly enhanced with the extension of heat treatment time, i.e., the optimal heat treatment duration is 10 h. Therefore, based on the above analysis, it can be concluded that the heat treatment for 5 h is conducive to improving the catalytic activity, and extension of the treatment time to 10 h can provide robust stability, which outperforms most reported acidic OER electrocatalysts in landmark literatures ([Figure 4E](#); [Table S4](#)). In addition, bulk C-RuO₂ was prepared by the method similar to that of C-RuO₂-RuSe-10, except that polyvinylpyrrolidone (PVP) was not introduced during the synthesis ([Figure S30](#)). The excellent activity and ultra-long stability of bulk C-RuO₂ prove that morphology has little effect on stability ([Figure S31](#)). To deliver 10 mA cm⁻², only an overpotential of 249 mV is required, indicating that it is a general method for RuO₂-based catalysts. The different heat treatment temperatures of RuSe₂ HNSs prove that the acidic OER activity and stability of C-RuO₂-RuSe are extremely sensitive to the annealing temperature ([Figures S32–S34](#)). Significant inactivation occurred when Vulcan XC-72R C powder was not added, indicating that the formed interstitial C plays a key role in improving stability, but only the presence of Se is invalid ([Figure S35](#)). Additionally, rapid stability decline can be observed for the Se-free

catalyst, which could be due to the fact that C is difficult to be incorporated into RuO₂ to form interstitial C without the presence of Se (Figures S14 and S36).

Detailed characterizations of C-RuO₂-RuSe-10 after electrocatalysis are shown in Figure S37. We can see that the hollow nanospheres and the characteristic signals of RuO₂ were largely maintained, demonstrating that C-RuO₂-RuSe-10 exhibits excellent morphological and structural stability under the harsh electrocatalytic environment in acids (Figures S37A–S37C). The slight increase in interplanar spacing may be caused by the dissolution during the electrocatalytic process, which is consistent with the TEM-EDS analysis (Figures S37D and S37E). The uniform element distribution is proved by STEM-EDS elemental mappings, confirming that C, O, Ru, and Se elements still exist after electrocatalysis (Figure S37F). No significant valence changes can be found for Ru and Se by XAS analysis (Figure S38). However, the weak peak for Ru–Ru bonds disappeared, indicating that Ru has been dissolved during the catalytic process. Therefore, a time tracking experiment was performed to monitor the dissolution of Se and Ru in the stability test, where the dissolution of Se increased linearly, indicating that Se will indeed gradually dissolve during the electrocatalytic process (Figure S39). It is worth noting that the dissolution of Ru is relatively slow during the initial period of electrolysis, while the accelerated dissolution of Ru occurs with the extension of the electrocatalytic time.

DFT theoretical simulations

To gain insights into the enhanced OER performance of C-RuO₂-RuSe-10, density functional theory (DFT) calculations were performed. The reason for the improved reaction activity of C-RuO₂-RuSe-10 than that of RuO₂ can be understood by calculating the energy change of potential-determining steps (PDSs), the formation of *OOH, during the OER reaction.³² As shown in Figure 5A, the calculated ΔG for PDSs on RuO₂ and C-RuO₂-RuSe-10 are 2.02 and 1.782 eV, respectively, which indicates that interstitial C could obviously reduce energy barriers for boosting OER activities, being consistent with the experiment observed. Due to strongly oxidative operating conditions and corrosive electrolytes, it is commonly known that catalyst stability in acidic electrolytes plays an important role in the efficiency of OER electrocatalysts.³³ Theoretically, dissociation energy for lattice O that is directly coordinated to the Ru core can be a critical factor in determining the stability of the catalyst under acidic conditions for the modeled RuO₂ system.³⁴ As shown in Figure 5B, the dissociation energy of *O, ΔG_O , for the C-RuO₂ system is 0.8 eV higher than that on pure RuO₂ system, indicating that the lattice O atom is much harder to dissociate in the electrolyte solution. This will be effectively beneficial to enhance the stability of RuO₂ during the reaction process. The Ru–O gap can clearly be elongated by 0.11 Å because of the interstitial C atom, which is in strong alignment with the EXAFS experiment, leading to the improved lattice O stability in C-RuO₂-RuSe-10 due to the additional bonding activity between adjacent bonded C and lattice O. Additionally, the structure-activity relationship of C-RuO₂-RuSe-10 and RuO₂ is depicted in Figure 5C. Compared with RuO₂, the elongated Ru–O bonds of C-RuO₂-RuSe-10 by the formation of interstitial C will optimize the ΔG of PDS, thereby reducing the overpotential during the OER process. More importantly, the binding energy for *O will be enhanced, thus leading to a significant increase in stability.

Conclusions

In summary, we have demonstrated that the stability and activity of RuO₂ can be significantly improved by interstitial C engineering. The C-RuO₂-RuSe-10 has been obtained by controlling the evaporation and combustion process of Se and C of the C-supported RuSe₂ HNSs in air. The optimized C-RuO₂-RuSe exhibits an excellent OER activity while

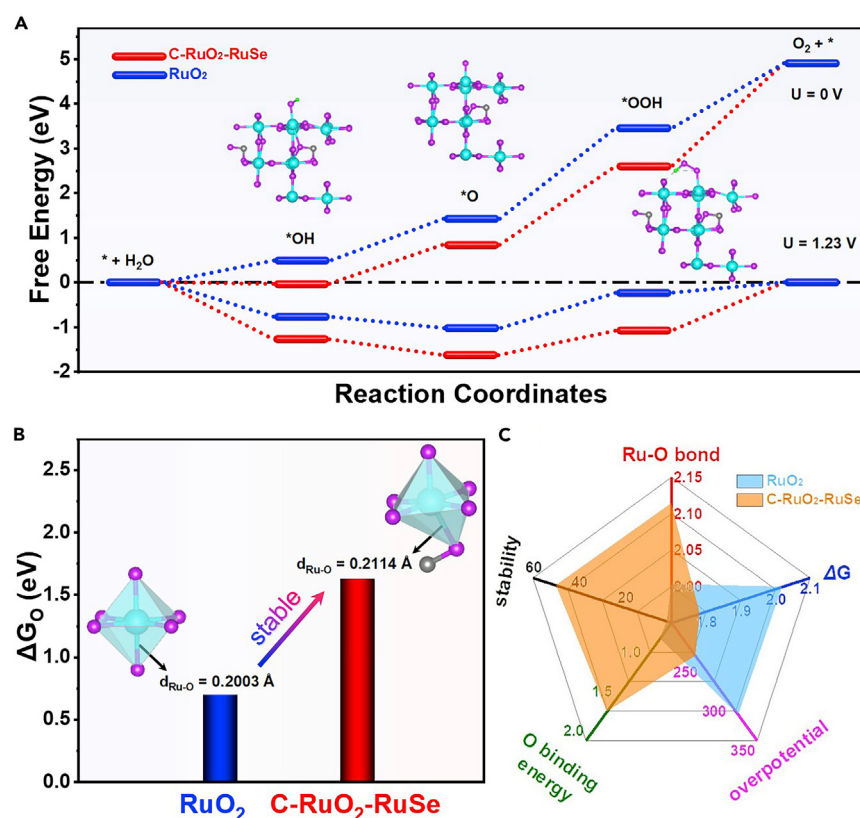


Figure 5. DFT

(A) The free energy profiles of the OER process on RuO₂ and C-RuO₂-RuSe-10 under the applied overpotential of 0 and 1.23 V (versus RHE), respectively; insets are the optimized intermediates during OER on C-RuO₂-RuSe-10.

(B) The calculated dissociation energy of *O in RuO₂ and C-RuO₂-RuSe-10; insets are the optimized octahedral models for RuO₂ and C-RuO₂-RuSe-10, showing the obvious Ru–O bond enlargement due to the interstitial C atom.

(C) Schematic diagram of OER activity and chemical energy. Sky blue color represents Ru, purple color represents O, green color represents H, and gray color represents C.

an enhanced stability of about 50 h was obtained. XAS measurements confirm that the C–O bonds formed by interstitial C can elongate the Ru–O bonds, thereby improving the activity and stability during the OER process. Theoretical calculations show that RuO₂ with interstitial C has higher *O binding energy and lower ΔG in PDSs, indicating that C-RuO₂-RuSe has better activity and stability in OER, which is consistent with the experimental observations. This work opens up a promising perspective for designing and constructing a new generation of high-performance electrocatalysts, thereby broadly expanding future materials research in various potential applications.

EXPERIMENTAL PROCEDURES

Resource availability

Lead contact

Further information and requests for resources should be directed to and will be fulfilled by the lead contact, Xiaoqing Huang (hxq006@xmu.edu.cn).

Materials availability

All materials generated in this study are available from the lead contact upon request.

Data and code availability

Data and code generated during this study are available from the lead contact upon request.

Chemicals

Hexaammineruthenium (III) chloride (Cl₃H₁₈N₆Ru, Ru 32.1%) was purchased from Alfa Aesar. Selenious acid (H₂SeO₃, 98%) was purchased from Sigma-Aldrich. Hydrazine hydrate aqueous solution (N₂H₄·H₂O, AR) and isopropanol (IPA, AR) were purchased from Sinopharm Chemical Reagent. Polyvinylpyrrolidone (PVP, average M.W. 58000) was purchased from J&K Scientific.

Preparation of RuSe₂ HNSs

In a typical preparation process, 7.7 mg of Cl₃H₁₈N₆Ru, 6.5 mg of H₂SeO₃, and 50.0 mg of PVP were added into a mixture containing 10.0 mL of H₂O and 0.12 mL of N₂H₄·H₂O. Then, the mixture was transferred into Teflon-sealed autoclave and maintained at 180°C for 12 h. After that, RuSe₂ HNSs were obtained by centrifugation and were washed with ethanol/acetone solution.

Preparation of C-RuO₂-RuSe

RuSe₂ HNSs were loaded on VC-X72 C (Ru loading of ~15 wt %, determined by ICP-AES) by sonicating for about 20 min in ethanol. Subsequently, the C-supported RuSe₂ HNSs were washed with ethanol/acetone solution. The products were annealed at 300°C in air for 0.5, 1, 5, 10, 20, and 30 h (denoted as C-RuO₂-RuSe-0.5, C-RuO₂-RuSe-1, C-RuO₂-RuSe-5, C-RuO₂-RuSe-10, C-RuO₂-RuSe-20, and C-RuO₂-RuSe-30, respectively). C-RuO₂-RuSe-10-250°C and C-RuO₂-RuSe-10-350°C were C-supported RuSe₂ HNSs annealed under air atmosphere at 250°C and 350°C for 10 h, respectively. The synthesis of RuO₂ NSs-10, Se-RuO₂-10, and bulk C-RuO₂ is the same as that of C-RuO₂-RuSe-10, except that H₂SeO₃, Vulcan XC-72R C, and PVP are not introduced, respectively.

Electrochemical measurement

Electrochemical data were collected on a CHI660 workstation (Chenhua, Shanghai) with a three-electrode system in 0.5 M H₂SO₄. The ink, including 195 µL of IPA and 5 µL of Nafion (5%), was dropped on the surface of the glassy C electrode (diameter: 5 mm) as the working electrode (loading amount: about 60 µg_{Ru}). A graphite rod and a SCE are used as the counter and reference electrode, respectively. All polarization curves are the average of the stable polarization curves scanned in three experiments with 95% iR compensation after 100 cycles of cyclic voltammograms (CVs).³⁵ In addition, the scan rate of the polarization curve was set to 5 mV s⁻¹ at a speed of 1600 r.p.m. The FE can be calculated as follows:

$$\text{FE (\%)} = \frac{4nF}{Q}$$

where Q is the total charge in the OER process, n is the number of moles of the product, and F is the Faraday constant. The gas products are detected by gas chromatograph (GC Agilent 7890B) with Ar as carrier gas.

DFT calculations

The quantum mechanics (QM) calculations were carried out using VASP software, version 5.4.4, with the Perdew, Burke, and Ernzerhof (PBE) flavor of DFT.³⁶ The projector augmented wave (PAW) method was used to account for core-valence interactions.^{37,38} The kinetic energy cutoff for plane wave expansions was set to 450 eV, and reciprocal space was sampled by the gamma-centered k-mesh with

a grid of $3 \times 3 \times 1$. The vacuum layer is at least 15 Å above the surface. The convergence criteria were 1×10^{-5} eV energy differences for solving the electronic wave function. The Methfessel-Paxton smearing of second order with a width of 0.1 eV was applied. All geometries (atomic coordinates) were converged to within 1×10^{-2} eV Å⁻¹ for maximal components of forces. A post-stage vdW DFT-D3 method with Becke-Jonson damping was applied.

Our model was built from a RuO₂ unit cell (one Ru atom bound to six oxygen atoms) with experimental lattice parameters of $a = b = 4.54$ Å and $c = 3.13$ Å. The detailed steps are as follows: first, RuO₂ (110) surface with three layers was built, and the lattice parameter was $a = 6.42$ Å, $b = 9.41$ Å, and $c = 23.39$ Å. The surface had two kinds of Ru sites: one site was saturated with six oxygen atoms and the other site bound with five oxygen atoms was the actual reaction site. The second C atom was dropped between the first layer and the second layer.

Adsorption behavior of *O, *OH, and *OOH intermediates for each catalyst and each model was optimized to convergence. ΔG for each OER step was calculated through the model of computational hydrogen electrode along with the equation as follows:

$$\Delta G = \Delta E_{DFT} + \Delta ZPE - T\Delta S$$

where ΔE_{DFT} , ΔZPE , and ΔS are the changes in DFT total energy, zero-point energy, and entropy from the initial state to the final state, respectively. Here, T means temperature; ΔZPE and ΔS can be obtained by the NIST-JANAF thermodynamics table for gaseous molecules³⁹ and by calculating the vibrational frequencies for the reactive intermediates, respectively. The entropy of the chemisorbed intermediates only takes the vibrational entropy into account. The dissociation energy of *O and ΔG_O is calculated as follows:

$$\Delta G_O = G_{sur} + (G_{H2O} - G_{H2}) - G(*_O)$$

G_{sur} refers to the surface energy without adsorbate; $G(*_O)$ refers to the energy that adsorbs the structure of *O intermediate; G_{H2O} and G_{H2} are the energy for water molecules and hydrogen molecules, respectively.

SUPPLEMENTAL INFORMATION

Supplemental information can be found online at <https://doi.org/10.1016/j.chempr.2022.02.003>.

ACKNOWLEDGMENTS

This work was financially supported by the Ministry of Science and Technology of China (2017YFA0208200 and 2016YFA0204100), the National Natural Science Foundation of China (22025108, 21903058, 22173066, 22103054, and 22105146), the Natural Science Foundation of Jiangsu Higher Education Institutions (17KJB150032 and BK20190810) and Jiangsu Province High-Level Talents (JNHB-106), the Project of Scientific and Technologic Infrastructure of Suzhou (Szs201708), the Priority Academic Program Development of Jiangsu Higher Education Institutions (PAPD), and start-up support from Xiamen University. The authors would like to thank SSRF (beamline 02B02), TLS (beamline 01C1), and BSRF (beamline1W1B) for the allocation of synchrotron beamtime. T.C. and H.Y. are supported by grants from start-up supports of Soochow University and T.C. by the Program for Jiangsu Specially Appointed Professors. H.Y. thanks the China Postdoctoral Science

Foundation (2019M660128) and Jiangsu Planned Projects for Postdoctoral Research Funds (2021K184B) for financial support. This work was partly supported by the Collaborative Innovation Center of Suzhou Nano Science & Technology, the 111 Project, and the Joint International Research Laboratory of Carbon-Based Functional Materials and Devices.

AUTHOR CONTRIBUTIONS

X.H. conceived and supervised the research. X.H. and J.W. designed the experiments. X.H., J.W., C.C., J.C., L.L., S.-C.H., Q.S., and L.Z. performed most of the experiments and data analysis. X.H., J.W., C.C., J.C., L.L., S.-C.H., Q.S., L.Z., and F.J. participated in various aspects of the experiments and discussions. Q.Z., F.M., and L.G. performed TEM experiments. Q.Y., H.Y., and T.C. performed DFT simulations. X.H., J.W., Q.Y., and F.J. wrote the paper. J.W., C.C., and Q.Y. contributed equally. All authors discussed the results and commented on the manuscript.

DECLARATION OF INTERESTS

The authors declare no competing interests.

Received: August 4, 2021

Revised: September 23, 2021

Accepted: February 7, 2022

Published: March 2, 2022

REFERENCES

- Li, L., Wang, P., Shao, Q., and Huang, X. (2020). Metallic nanostructures with low dimensionality for electrochemical water splitting. *Chem. Soc. Rev.* 49, 3072–3106.
- Wu, Z., Zhao, Y., Jin, W., Jia, B., Wang, J., and Ma, T. (2021). Recent progress of vacancy engineering for electrochemical energy conversion related applications. *Adv. Funct. Mater.* 31, 2009070.
- Wei, C., Sun, S., Mandler, D., Wang, X., Qiao, S.Z., and Xu, Z.J. (2019). Approaches for measuring the surface areas of metal oxide electrocatalysts for determining their intrinsic electrocatalytic activity. *Chem. Soc. Rev.* 48, 2518–2534.
- Zang, Y., Niu, S., Wu, Y., Zheng, X., Cai, J., Ye, J., Xie, Y., Liu, Y., Zhou, J., Zhu, J., et al. (2019). Tuning orbital orientation endows molybdenum disulfide with exceptional alkaline hydrogen evolution capability. *Nat. Commun.* 10, 1217.
- Wu, Y., Liu, X., Han, D., Song, X., Shi, L., Song, Y., Niu, S., Xie, Y., Cai, J., Wu, S., et al. (2018). Electron density modulation of NiCo₂S nanowires by nitrogen incorporation for highly efficient hydrogen evolution catalysis. *Nat. Commun.* 9, 1425.
- Gao, W., Xia, Z., Cao, F., Ho, J.C., Jiang, Z., and Qu, Y. (2018). Comprehensive understanding of the spatial configurations of CeO₂ in NiO for the electrocatalytic oxygen evolution reaction: embedded or surface-loaded. *Adv. Funct. Mater.* 28, 1706056.
- An, L., Huang, B., Zhang, Y., Wang, R., Zhang, N., Dai, T., Xi, P., and Yan, C.H. (2019). Interfacial defect engineering for improved portable zinc-air batteries with a broad working temperature. *Angew. Chem. Int. Ed. Engl.* 58, 9459–9463.
- Xiao, Z., Huang, Y.C., Dong, C.L., Xie, C., Liu, Z., Du, S., Chen, W., Yan, D., Tao, L., Shu, Z., et al. (2020). Operando identification of the dynamic behavior of oxygen vacancy-rich Co₃O₄ for oxygen evolution reaction. *J. Am. Chem. Soc.* 142, 12087–12095.
- Liu, Z., Wang, G., Zhu, X., Wang, Y., Zou, Y., Zang, S., and Wang, S. (2020). Optimal geometrical configuration of cobalt cations in spinel oxides to promote oxygen evolution reaction. *Angew. Chem. Int. Ed. Engl.* 59, 4736–4742.
- Wang, J., Ji, Y., Yin, R., Li, Y., Shao, Q., and Huang, X. (2019). Transition metal-doped ultrathin RuO₂ networked nanowires for efficient overall water splitting across a broad pH range. *J. Mater. Chem. A* 7, 6411–6416.
- Meng, G., Sun, W., Mon, A.A., Wu, X., Xia, L., Han, A., Wang, Y., Zhuang, Z., Liu, J., Wang, D., et al. (2019). Strain regulation to optimize the acidic water oxidation performance of atomic-layer IrO_x. *Adv. Mater.* 31, 1903616.
- Shang, C., Cao, C., Yu, D., Yan, Y., Lin, Y., Li, H., Zheng, T., Yan, X., Yu, W., Zhou, S., and Zheng, J. (2019). Electron correlations engineer catalytic activity of pyrochlore iridates for acidic water oxidation. *Adv. Mater.* 31, 1805104.
- Seitz, L.C., Dickens, C.F., Nishio, K., Hikita, Y., Montoya, J., Doyle, A., Kirk, C., Vojvodic, A., Hwang, H.Y., Norskov, J.K., and Jaramillo, T.F. (2016). A highly active and stable IrO_x/SrIrO₃ catalyst for the oxygen evolution reaction. *Science* 353, 1011–1014.
- Cui, X., Ren, P., Ma, C., Zhao, J., Chen, R., Chen, S., Rajan, N.P., Li, H., Yu, L., Tian, Z., and Deng, D. (2020). Robust interface Ru centers for high-performance acidic oxygen evolution. *Adv. Mater.* 32, 1908126.
- Gao, J., Xu, C.Q., Hung, S.F., Liu, W., Cai, W., Zeng, Z., Jia, C., Chen, H.M., Xiao, H., Li, J., et al. (2019). Breaking long-range order in iridium oxide by alkali ion for efficient water oxidation. *J. Am. Chem. Soc.* 141, 3014–3023.
- Kötz, R., Stucki, S., Scherson, D., and Kolb, D.M. (1984). In-situ identification of RuO₄ as the corrosion product during oxygen evolution on ruthenium in acid media. *J. Electroanal. Chem.* 172, 211–219.
- Su, J., Ge, R., Jiang, K., Dong, Y., Hao, F., Tian, Z., Chen, G., and Chen, L. (2018). Assembling ultrasmall copper-doped ruthenium oxide nanocrystals into hollow porous polyhedra: highly robust electrocatalysts for oxygen evolution in acidic media. *Adv. Mater.* 30, 1801351.
- Hao, S., Liu, M., Pan, J., Liu, X., Tan, X., Xu, N., He, Y., Lei, L., and Zhang, X. (2020). Dopants fixation of ruthenium for boosting acidic oxygen evolution stability and activity. *Nat. Commun.* 11, 5368.
- Shan, J., Guo, C., Zhu, Y., Chen, S., Song, L., Jaroniec, M., Zheng, Y., and Qiao, S.Z. (2019). Charge-redistribution-enhanced nanocrystalline Ru@IrO_x electrocatalysts for oxygen evolution in acidic media. *Chem* 5, 445–459.
- Yao, Y., Hu, S., Chen, W., Huang, Z.Q., Wei, W., Yao, T., Liu, R., Zang, K., Wang, X., Wu, G., et al. (2019). Engineering the electronic structure of single atom Ru sites via compressive strain boosts acidic water oxidation electrocatalysis. *Nat. Catal.* 2, 304–313.

21. Ge, R., Li, L., Su, J., Lin, Y., Tian, Z., and Chen, L. (2019). Ultrafine defective RuO₂ electrocatalyst integrated on carbon cloth for robust water oxidation in acidic media. *Adv. Energy Mater.* 9, 1901313.
22. Jiang, Q., Kurra, N., Alhabeb, M., Gogotis, Y., and Alshareef, H.N. (2018). All pseudocapacitive MXene-RuO₂ asymmetric supercapacitors. *Adv. Energy Mater.* 8, 1703043.
23. Lin, Y., Tian, Z., Zhang, L., Ma, J., Jiang, Z., Deibert, B.J., Ge, R., and Chen, L. (2019). Chromium-ruthenium oxide solid solution electrocatalyst for highly efficient oxygen evolution reaction in acidic media. *Nat. Commun.* 10, 162.
24. Kim, J., Shih, P.C., Tsao, K.C., Pan, Y.T., Yin, X., Sun, C.J., and Yang, H. (2017). High-performance pyrochlore-type yttrium ruthenate electrocatalyst for oxygen evolution reaction in acidic media. *J. Am. Chem. Soc.* 139, 12076–12083.
25. Zhang, L., Jang, H., Liu, H., Kim, M.G., Yang, D., Liu, S., Liu, X., and Cho, J. (2021). Sodium-decorated amorphous/crystalline RuO₂ with rich oxygen vacancies: a robust pH-universal oxygen evolution electrocatalyst. *Angew. Chem. Int. Ed. Engl.* 60, 18821–18829.
26. Hu, Z., Lips, H.V., Golden, M.S., and Fink, J. (2000). Multiplet effects in the Ru L_{2,3} x-ray absorption spectra of Ru(IV) and Ru(V) compounds. *Phys. Rev. B* 61, 8–15.
27. Zhou, J., Wang, J., Fang, H., Wu, C., Cutler, J.N., and Sham, T.K. (2010). Nanoscale chemical imaging and spectroscopy of individual RuO₂ coated carbon nanotubes. *Chem. Commun.* 46, 2778–2780.
28. Frati, F., Hunault, M.O.J.Y., and de Groot, F.M.F. (2020). Oxygen K-edge x-ray absorption spectra. *Chem. Rev.* 120, 4056–4110.
29. Wang, D., Yang, J., Li, X., Geng, D., Li, R., Cai, M., Sham, T.K., and Sun, X. (2013). Layer by layer assembly of sandwiched graphene/SnO₂ nanorod/carbon nanostructures with ultrahigh lithium ion storage properties. *Energy Environ. Sci.* 6, 2900–2906.
30. Ray, S.C. (2018). Nitrogenated carbon nanotubes functionalized with chlorine and oxygen: electronic and magnetic properties for electronic/magnetic device applications. *Front. Res. Today* 1, 1006.
31. Wang, J., Han, L., Huang, B., Shao, Q., Xin, H.L., and Huang, X. (2019). Amorphization activated ruthenium-tellurium nanorods for efficient water splitting. *Nat. Commun.* 10, 5692.
32. Viswanathan, V., Hansen, H.A., Rossmeisl, J., and Nørskov, J.K. (2012). Unifying the 2e⁻ and 4e⁻ reduction of oxygen on metal surfaces. *J. Phys. Chem. Lett.* 3, 2948–2951.
33. Sun, H., Yan, Z., Liu, F., Xu, W., Cheng, F., and Chen, J. (2019). Self-supported transition-metal-based electrocatalysts for hydrogen and oxygen evolution. *Adv. Mater.* 32, e1806326.
34. Grimaud, A., Diaz-Morales, O., Han, B., Hong, W.T., Lee, Y.L., Giordano, L., Stoezinger, K.A., Koper, M.T.M., and Shao-Horn, Y. (2017). Activating lattice oxygen redox reactions in metal oxides to catalyse oxygen evolution. *Nat. Chem.* 9, 457–465.
35. Wei, C., Rao, R.R., Peng, J., Huang, B., Stephens, I.E.L., Risch, M., Xu, Z.J., and Shao-Horn, Y. (2019). Recommended practices and benchmark activity for hydrogen and oxygen electrocatalysis in water splitting and fuel cells. *Adv. Mater.* 31, 1806296.
36. Kresse, G., and Furthmüller, J. (1996). Efficient iterative schemes for ab initio total-energy calculations using a plane-wave basis set. *Phys. Rev. B Condens. Matter* 54, 11169–11186.
37. Perdew, J.P., Chevary, J.A., Vosko, S.H., Jackson, K.A., Pederson, M.R., Singh, D.J., and Fiolhais, C. (1992). Atoms, molecules, solids, and surfaces: applications of the generalized gradient approximation for exchange and correlation. *Phys. Rev. B Condens. Matter* 46, 6671–6687.
38. Perdew, J.P., Chevary, J.A., Vosko, S.H., Jackson, K.A., Pederson, M.R., Singh, D.J., and Fiolhais, C. (1993). Erratum: atoms, molecules, solids, and surfaces: applications of the generalized gradient approximation for exchange and correlation. *Phys. Rev. B Condens. Matter* 48, 4978.
39. Chase, M.W., Jr. (1998). NIST JANAF Thermochemical Tables (American Institute of Physics).